JOURNAL OF SOLID STATE CHEMISTRY 103, 139–151 (1993)

Crystal Structures and Magnetic Properties of MV_3O_7 (M = Cd, Ca, Sr) with Square Pyramidal V(IV)

GUO LIU AND J. E. GREEDAN

Institute for Materials Research, McMaster University, Hamilton, Ontario, Canada L8S 4M1

Received March 31, 1992; in revised form August 14, 1992; accepted August 17, 1992

Crystal structures of CdV_3O_7 and SrV_3O_7 are refined using X-ray powder diffraction data for CdV_3O_7 and a combination of neutron and X-ray powder data for SrV_3O_7. The pseudo two-dimensional feature and possible chain formation of the crystal structures are described. Magnetic properties are examined in the temperature range from 5 to 300 K and magnetic susceptibility data of these insulating antiferromagnets are analyzed according to a linear chain (1-D) Heisenberg model. © 1993 Academic Press, Inc.

Introduction

Efforts to search for new superconductors containing noncopper transition metals have led to the investigation of oxides of the d^1 V(IV), a one-electron analog of the one-hole d^9 Cu(II). Superconductivity in vanadium oxides was claimed but not confirmed, and its likelihood has been questioned recently (*1*). However, these investigations did result in the synthesis and characterization of novel V(IV) oxides with interesting magnetic and electrical properties in the past few years. The K_2NiF_4-type semiconductive Sr_2VO_4 (*2–4*) and the so-called R–P (Ruddlesden–Popper) phases, metallic $Sr_3V_2O_7$ (*2*, *3*) and $Sr_4V_3O_{10}$ (*3*, *5*, *6*) are examples of new V(IV) oxides with octahedral VO_6^{8-} coordination polyhedra and perovskite-derived crystal structures common to many of the La–Ba–Cu–O superconductors. The recently reported metastable high-temperature form of Sr_2VO_4 is an interesting $S = \frac{1}{2}$ magnetic dimer (*7*) and its crystal structure appears to consist of $V_2O_8^{8-}$ dimers with tetrahedral VO_4^{4-} and trigonal bipyramidal VO_5^{6-} (*8*).

It is interesting to note that vanadium-rich oxides of the MV_nO_{2n+1}-type (n = 2, 3, 4 for M = Ca and n = 3, 5 for M = Sr) which were first reported by Bouloux and Galy consist of VO_5^{6-} square pyramids (*9–11*). Square pyramidal coordination is also found in most superconducting Cu(II) oxides (*12*). Thus these five-coordinated V(IV) oxides share another common structural feature with Cu(II) oxides. The MV_3O_7-type compounds are especially interesting because of the phase stability in a relatively wide range of different-sized M cations (M = Cd, Ca, and Sr) (*9*) and the lack of complete structural and physical property characterizations of these compounds. The crystal structure of CaV_3O_7 was determined using single-crystal X-ray data (*9*). It is centrosymmetric with the space group *Pnam* (no. 62). Although no detailed structural data for CdV_3O_7 and SrV_3O_7 were reported, they were assigned to the noncentrosymmetric space group $Pna2_1$ based on piezoelectric

0022-4596/93 $5.00

measurements (*9*). In this work crystal structure refinements of CdV_3O_7 and SrV_3O_7 and magnetic properties of all these MV_3O_7 phases (M = Cd, Ca, Sr) are presented.

Experimental

Sample Preparation

CdV_3O_7. Stoichiometric amounts of CdO (Allied Chemicals, 99%, heated at 550°C in flowing argon for 8 hrs before use), V_2O_5 (Cerac, 99.9%) and V_2O_3 obtained by hydrogen reduction of V_2O_5 at 650–750°C were mixed according to the equation

$$4CdO + 3V_2O_3 + 3V_2O_5 \rightarrow 4CdV_3O_7.$$

The mixture was ground intimately, pelleted and sealed in a quartz tube under a 10^{-4}-Torr pressure. The sealed tube was then heated at 3°C/min to 700°C, soaked for 24 hr, and finally air-quenched or cooled slowly in the oven.

CaV_3O_7. Two methods were used. In the first method a stoichiometric mixture of CaO prepared by decomposition of $CaCO_3$ (Mallinckrodt Analytical Reagent) at 920°C and VO_2 made from a V_2O_3 and V_2O_5 1 : 1 mixture at 700°C in quartz was ground in an argon-filled glove box, loaded into a press, taken out of the glove box and pelleted rapidly, and then sealed in evacuated quartz. The quartz tube was heated at 900°C for 24 hr and air quenched. In the second method, $Ca_2V_2O_7$ was first made by heating a $2CaCO_3 + V_2O_5$ mixture at 900°C for 20–24 hr. Then a mixture of $Ca_2V_2O_7$, V_2O_3, and V_2O_5 weighed according to the equation

$$2Ca_2V_2O_7 + 3V_2O_3 + V_2O_5 \rightarrow 4CaV_3O_7$$

was ground intimately in air, pelleted, and sealed in quartz. The heating procedure is the same as that in the first method.

SrV_3O_7. The same two methods as for the synthesis of CaV_3O_7 were used. SrO was prepared by thermal decomposition of $SrCO_3$ at 1400°C. Sealed tubes were heated at 950°C for 24 hr and cooled down slowly.

Thermogravimetrical analysis (TGA) was performed with a Netzsch STA 409 Thermal Analyzer in flowing O_2 atmosphere at a heating rate of 5°C/min to 700°C.

X-ray and Neutron Diffraction

All specimens were examined routinely using a Guinier–Hägg camera (IRDAB XDC700) with Cu $K\alpha 1$ radiation and a Si standard. Step-scanned X-ray powder diffraction data of CdV_3O_7 suitable for profile refinement were collected in the range $15° < 2\theta < 90°$ using a Nicolet I2 diffractometer and Cu $K\alpha$ radiation, entrance beam soller collimator, exit beam monochromator, and a scintillation counter. Data collection conditions are summarized in Table I. Powder X-ray diffraction data were also collected for SrV_3O_7, but with a sintered pellet directly from the sealed tube reaction. Neutron diffraction data for powder SrV_3O_7 were collected at the McMaster Nuclear Reactor using 1.3913 Å neutrons obtained by reflection from a Cu [200] monochromator. Due to the strong absorption of neutrons by cadmium, suitable neutron powder data for CdV_3O_7 can not be collected. The X-ray data refinement was effected on a VAX computer using LHPM1 of Hill and Howard (*13*), which is a modified version of DBW3.2 due to Wiles and Young (*14*). Details of the neutron data collection and refinement methods have been described previously (*15*).

Magnetic Susceptibility Measurement

Susceptibility data were obtained using a Quantum Design SQUID magnetometer in the temperature range 5 to 300 K using sintered pellet specimens at applied magnetic fields of 1000–2000 Oe. Diamagnetic corrections were applied. Magnetic susceptibilities were evaluated based on per mole vanadium.

Results and Discussion

According to the Guinier X-ray diffraction results, CdV_3O_7 and CaV_3O_7 prepared

TABLE I

DATA COLLECTION CONDITIONS AND REFINEMENT DETAILS ($Z = 4$)

Compound	CdV_3O_7 (X-ray)	CaV_3O_7 (9)	SrV_3O_7 Neutron	SrV_3O_7 X-ray
Space group	*Pnam*	*Pnam*	*Pnam*	
Cell parameters				
a	10.3004(3)	10.459(8)	10.631(3)	10.633(1)
b	5.2906(1)	5.295(5)	5.301(1)	5.2975(7)
c	10.3227(3)	10.382(8)	10.529(3)	10.529(1)
2θ Range (°)	15–90		10–92	15–75
Step size (°)	0.020		0.10	0.020
Counting time (sec)	15		—	20
Preferred orientation parameter G_1	0.09(1)[a]		0.18(2)[b]	~0.0[a]
Overall temperature factor	—		—	0.12(8)
Nuclear R_N/Bragg R_B (%)	9.35		9.86	9.55
Weighted profile R_{WP} (%)	7.62		6.49	7.69
Profile R_P (%)	6.02		4.86	5.80
Expected R_E (%)	4.12		2.92	5.12
No. of profile points N	3749		821	3000
No. of parameters refined	33		32	32
Independent reflections	298		369	171

Note. $R_N = R_B = \Sigma |I_{obs} - I_{cal}|/\Sigma I_{obs}$; $R_{WP} = \{[\Sigma w(Y_{obs} - Y_{cal}/c)^2]/\Sigma w Y_{obs}^2\}^{1/2}$; $R_P = \Sigma |Y_{obs} - Y_{cal}/c|/\Sigma Y_{obs}$; $R_E = [(N - P)/\Sigma w Y_{obs}^2]^{1/2}$.

[a] Defined as $I_{corr} = I_{obs}[G_2 + (1 - G_2)\exp(-G_1\alpha^2)]$, where α is the acute angle between the scattering vector and the fiber axis direction. The fiber axis direction is expressed in reciprocal space. Here it is (0 1 1). Note G_2 is usually set to 0.0. $G_1 > 1.5$ for a pulverized SrV_3O_7 specimen tested.

[b] Defined as $I_{corr} = I_{obs}\exp(-G_1\alpha^2)$. The fiber axis direction is expressed as Miller indices of the normal to the surface of the plate-like crystals. Here it is (1 0 0).

by both methods described above were phase pure. Observed d-spacings matched those reported for CdV_3O_7 and CaV_3O_7 (9). The second method for the synthesis of CaV_3O_7 is better than the first one because the former method avoided the use of moisture sensitive CaO. Pure SrV_3O_7 is hard to prepare. In most cases the product was contaminated by an unidentified phase. The best sample was obtained as a phase pure material in small quantity (1 ~ 2 g) from an $SrO + 3VO_2$ mixture using freshly fired SrO and when the $SrO + 3VO_2$ mixture was pressed rapidly on a dry winter day. This phase pure sample of SrV_3O_7 was used for the magnetic susceptibility measurement. Observed d-spacings also matched those reported for SrV_3O_7 (9).

All three compounds are colored. CdV_3O_7 is yellow, CaV_3O_7 greenish-yellow, and SrV_3O_7 reddish-brown. This is in contrast to other known V(IV) oxides which are normally black. Pure specimens of CdV_3O_7, CaV_3O_7 and SrV_3O_7 are insulators. The contaminated SrV_3O_7 specimen has a lower resistance which decreases with increasing degree of contamination. TGA results suggest that the three compounds are stable in oxygen up to 400°C with a complete oxidation at ~600°C, and the specimens are nearly stoichiometric. Assuming that vanadium is oxidized to V(V) in the final product, the weight gain can be used to estimate the original composition. CdV_3O_7: calc. 6.36%, obs. 6.50 ± 0.09% ($CdV_3O_{6.97\pm0.05}$); CaV_3O_7: calc. 7.87%, obs. 7.91 ± 0.12%.

TABLE II

ATOMIC PARAMETERS FOR CdV_3O_7 FROM POWDER X-RAY DATA

Atom	Site	x	y	z	B(Å^2)
Cd	4(c)	0.4157(2)	0.2031(5)	0.25	1.12(5)
V(1)	8(d)	0.1858(3)	0.2216(9)	0.0221(3)	1.35(7)
V(2)	4(c)	0.2119(3)	0.708(1)	0.25	1.35(7)
O(1)	8(d)	0.286(1)	0.478(2)	0.121(1)	0.6(1)
O(2)	8(d)	0.273(1)	0.948(2)	0.120(1)	0.6(1)
O(3)	8(d)	0.0407(8)	0.237(3)	0.0691(8)	0.6(1)
O(4)	4(c)	0.055(1)	0.697(3)	0.25	0.6(1)

($CaV_3O_{6.99\pm0.05}$); SrV_3O_7: calc. 6.81%, obs. 7.13 ± 0.11% ($SrV_3O_{6.93\pm0.05}$).

Crystal Structures

Data collection conditions and refinement details are summarized in Table I. Initially the centrosymmetric space group (*Pnam*) was assumed and atomic parameters of CaV_3O_7 from single-crystal data (*9*) were used as starting values for the refinement of the CdV_3O_7 and SrV_3O_7 structures. Later the noncentrosymmetric space group ($Pna2_1$) was tested, but positional parameters had enormously high standard deviations with final R factors nearly the same as those for the centrosymmetric space group. Therefore, the space group $Pna2_1$ was rejected.

CdV_3O_7. Atomic parameters are listed in Table II. The observed, calculated and difference profiles are plotted in Fig. 1. The profile fit is seen to be excellent. Bond distances, including nearest V–V distances, and selected bond angles of CdV_3O_7 are listed in Table IV together with those of CaV_3O_7 and SrV_3O_7 for comparison.

It is worth noting that the refined a-axis for CdV_3O_7 is actually the previously assigned c-axis. Therefore, the a-axis is

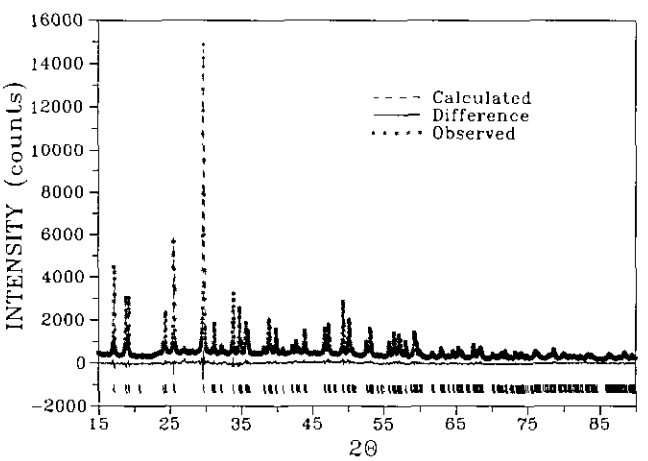

FIG. 1. Observed, calculated, and difference X-ray powder pattern of CdV_3O_7. Bragg peak positions are marked in the lower level as bars.

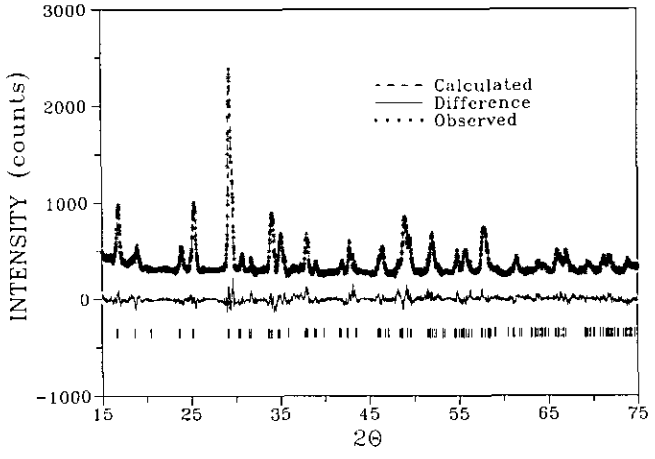

FIG. 2. Observed, calculated, and difference X-ray powder pattern of SrV_3O_7.

shorter than the c-axis. This result is the reverse order of that for CaV_3O_7 and SrV_3O_7 whose a-axes are longer than their c-axes.

SrV_3O_7. X-ray and neutron profiles are plotted in Figs. 2 and 3, respectively. Atomic parameters derived from both data sets are listed in Table III. Due to the existence of a small amount of unidentified impurity in the samples used for data collection, the profile fits for SrV_3O_7, both with X-ray and neutron data, are not as good as those for CdV_3O_7 even with a few non-overlapping peaks deleted. The relatively high R_B for the neutron data is believed to be largely the result of this effect.

Pulverized SrV_3O_7 has a strong tendency for preferred orientation along the fiber axis (1 0 0), the direction normal to the surface of the plate-like crystals. The effect is so severe in the case of the powder X-ray experiment that refinement using X-ray data obtained with pulverized specimens will not

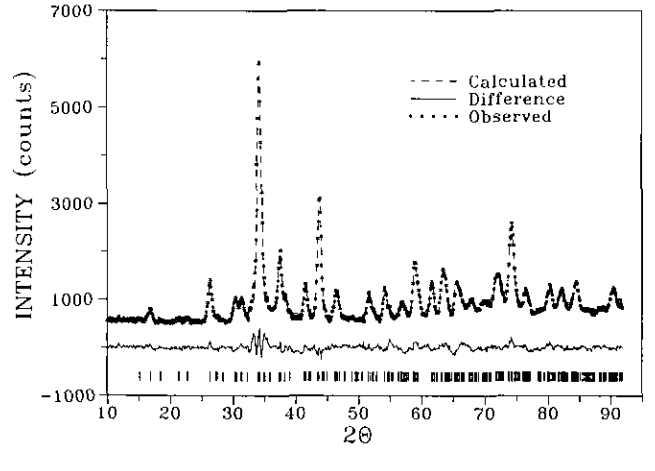

FIG. 3. Observed, calculated, and difference neutron powder pattern of SrV_3O_7.

TABLE III

ATOMIC PARAMETERS FOR SrV_3O_7 FROM NEUTRON AND X-RAY (IN SQUARE BRACKETS) POWDER DIFFRACTION DATA

Atom	Site	x	y	z	B(Å^2)
Sr	4(c)	0.427(1)	0.226(5)	0.25	2.5(4)
		[0.4263(6)]	[0.228(2)]	[0.25]	—
V(1)	8(d)	[0.1836(7)]	[0.276(2)]	[0.0206(5)]	—
V(2)	4(c)	[0.2118(8)]	[0.757(4)]	[0.25]	—
O(1)	8(d)	0.2798(9)	0.510(5)	0.112(2)	0.3(1)
		[0.281(3)]	[0.488(6)]	[0.118(4)]	—
O(2)	8(d)	0.262(1)	0.998(5)	0.120(1)	0.3(1)
		[0.288(4)]	[0.958(6)]	[0.114(4)]	—
O(3)	8(d)	0.0333(9)	0.262(4)	0.0425(8)	0.3(1)
		[0.055(3)]	[0.206(6)]	[0.067(1)]	—
O(4)	8(d)	0.057(1)	0.761(5)	0.25	0.3(1)
		[0.068(4)]	[0.807(9)]	[0.25]	—

converge even with a large preferred orientation correction (see Table I for details). Fortunately we were able to identify one sintered pellet which did not exhibit apparent preferred orientation. Preferred orientation was observed for the powder neutron data as well but the parameter G_1 of 0.18(2) is significantly smaller than that (>1.5) for the powder X-ray data as one would expect because of the large amount (~6 g) of sample used in the neutron scattering experiment. Preferred orientation along the same axis was also observed for CdV_3O_7 and CaV_3O_7, but it is far less prominent than that of SrV_3O_7.

Atomic parameters of V(1) and V(2) derived from the X-ray refinement were used in the neutron refinement and held fixed. Bond distances and angles from the neutron diffraction data are listed in Table IV. Those calculated from X-ray data are not listed because positional parameters for the light oxygen atoms derived from X-ray data are less reliable than those from neutron data as can be seen from the higher standard deviations for the oxygen atoms in the X-ray refinement (Table III). Positional parameters for the heavy atoms, Sr and V, can be considered quantitatively valid.

The refinement results confirm that both CdV_3O_7 and SrV_3O_7 are isostructural with CaV_3O_7. In fact, there is very little shift in atomic positions of CdV_3O_7 as compared to those of CaV_3O_7 which is not surprising given the similar size of the M^{2+} ions. Deviations are apparent for SrV_3O_7. There are two crystallographically distinct vanadium atoms, both of which are coordinated to five oxygens in a square pyramidal fashion. It is clear from Table IV that the axial V–O bonds, which are about 0.35 Å shorter than the basal V–O bonds, must involve some degree of double bonding. The square pyramids of CdV_3O_7 and CaV_3O_7 are more regular than those of SrV_3O_7 because basal V–O bonds of CdV_3O_7 and CaV_3O_7, which are in the range 1.95–1.99 Å, are nearly of equal distances while those of SrV_3O_7 have rather large differences. The basal V(1)–O bonds of SrV_3O_7 include three long bonds (1.98–2.02 Å) and one short (1.87 Å) bond, and the basal V(2)–O bonds include two long bonds (2.09 Å) and two short (1.94 Å) ones. The average V(1)–O and V(2)–O bond distances of 1.89–1.90 Å remain nearly unchanged for the three compounds except for the V(2)–O of SrV_3O_7 which is slightly longer (1.94 Å).

The difference between the VO_5^{6-} polyhedra and the CuO_5^{8-} square pyramids found

TABLE IV

BOND AND NEAREST V–V DISTANCES (Å) AND SELECTED BOND ANGLES (°)

MV_3O_7	CdV_3O_7	CaV_3O_7	SrV_3O_7
M^i–O(1)^i	2.38(1)	2.44(2)	2.61(3)
M^i–O(1)^{vii}	2.38(1)	2.44(2)	2.61(3)
M^i–O(2)^i	2.40(1)	2.41(3)	2.53(3)
M^i–O(2)^{vii}	2.40(1)	2.41(3)	2.53(3)
M^i–O(3)^{ii}	2.290(9)	2.36(2)	2.46(1)
M^i–O(3)^{viii}	2.290(9)	2.36(2)	2.46(1)
M^i–O(4)^{ii}	2.56(1)	2.60(4)	2.93(3)
Average M–O	2.386	2.43	2.59
V(1)^i–O(1)^i	1.99(1)	1.96(2)	1.87(2)
V(1)^i–O(2)^i	1.98(1)	1.96(3)	1.99(2)
V(1)^i–O(1)^{iv}	1.98(1)	1.97(2)	2.02(2)
V(1)^i–O(2)^{iv}	1.95(1)	1.95(3)	1.98(2)
V(1)^i–O(3)^i	1.574(9)	1.59(2)	1.616(9)
Average V(1)–O	1.89	1.89	1.90
V(2)^i–O(1)^i	1.96(1)	1.98(2)	2.09(2)
V(2)^i–O(1)^{vii}	1.96(1)	1.98(2)	2.09(2)
V(2)^i–O(2)^i	1.95(1)	1.98(3)	1.94(3)
V(2)^i–O(2)^{vii}	1.95(1)	1.98(3)	1.94(3)
V(2)^i–O(4)^i	1.61(1)	1.57(4)	1.64(1)
Average V(2)–O	1.89	1.90	1.94
V(1)^i–V(2)^i	3.497(7)	3.536(8)	3.525(15)
V(1)^i–V(2)$^{i\,a}$	3.604(7)	3.605(8)	3.673(16)
V(1)^i–V(1)^{iv}	2.992(3)	2.982(5)	3.034(1)
V(1)^i–V(1)$^{iv\,a}$	2.992(3)	2.982(5)	3.034(1)
V(1)^i–V(2)$^{vi\,a}$	3.001(3)	3.002(6)	3.060(3)
V(1)^i–O(1)^i–V(1)^{iv}	97.96(6)	98.9(9)	102.2(8)
V(1)^i–O(1)^i–V(2)^i	124.9(8)	128.0(11)	125.8(6)
V(1)^{iv}–O(1)^i–V(2)^i	99.3(5)	99.2(12)	96.2(11)
V(1)^i–O(2)^i–V(1)^{iv}	99.3(6)	99.4(14)	99.6(6)
V(1)^i–O(2)^i–V(2)^i	133.2(6)	132.1(12)	138.1(8)
V(1)^{iv}–O(2)^i–V(2)^i	100.8(5)	99.5(12)	102.5(13)

Note. Conventions for equivalent positions (space group *Pnam*, no. 62): i. (x, y, z); ii. $(0.5 + x, 0.5 - y, 0.5 - z)$; iii. $(-x, -y, 0.5 + z)$; iv. $(0.5 - x, 0.5 + y, -z)$; v. $(-x, -y, -z)$; vi. $(0.5 - x, 0.5 + y, 0.5 + z)$; vii. $(x, y, 0.5 - z)$; viii. $(0.5 + x, 0.5 - y, z)$.

[a] Atoms from neighboring unit cells.

in *Ln*–Ba–Cu–O systems is obvious. In the Cu oxides a square pyramid is formed when one axial oxygen is removed from a CuO_6 octahedron and thus Cu is located nearly in the basal oxygen plane with O–Cu–O bond angles close to 90° and 180° (*12*) while V is displaced from the basal plane(s) towards the axial oxygens, resulting in short axial V–O bonds.

The structure of CaV_3O_7 has been described previously (*9*). Some features are worthy of further examination to aid in the understanding of the magnetic behavior of these compounds. The structure of SrV_3O_7 is projected down the *b*- and *a*-axes in Figs. 4 and 5, respectively. This structure can probably be best described as a pseudo-two-dimensional network consisting of VO_5^{6-} square pyramids parallel to the *YZ* plane. Neighboring planes are separated by SrO_7 polyhedra. As can be seen in Fig. 4 the separation of the pseudo-planes is rather large. Figure 5 is a projection of such a single layer with $0.0 \leq x < 0.5$. The adjacent second layer ($0.5 \leq x < 1.0$) is so similar to the first one that like atoms from both layers almost overlap on the same projection. This feature can be seen clearly in Fig. 4. It is believed that the two-dimensional feature is responsible for the observed preferred orientation behavior because the fiber axis (1 0 0) is the normal of the pseudo two-dimensional network. However, it is unclear why pulverized forms of CdV_3O_7 and CaV_3O_7 do not display preferred orientation as strongly as SrV_3O_7.

The arrangements of the square pyramids within each layer can be viewed from two different perspectives. In the first the square pyramids are linked by edge sharing to form chains running in the direction parallel to the *b*-axis with the vertices pointing up and down alternately, and the chains are cross-linked by individual square pyramids also by edge sharing. In the second every three square pyramids form a trimeric chain unit of $[V_3O_{11}]^{10-}$ again by edge sharing with alternate up and down vertices but running parallel to the *c*-axis, and these units are cross-linked by edge sharing with neighboring $[V_3O_{11}]^{10-}$ units.

Magnetic Properties

All three compounds have a broad susceptibility maximum which shifts regularly from ~35 K for CdV_3O_7 to ~110 K for SrV_3O_7 with increasing size of M^{2+} in MV_3O_7 (Table V). Although their crystal structures appear to be two-dimensional,

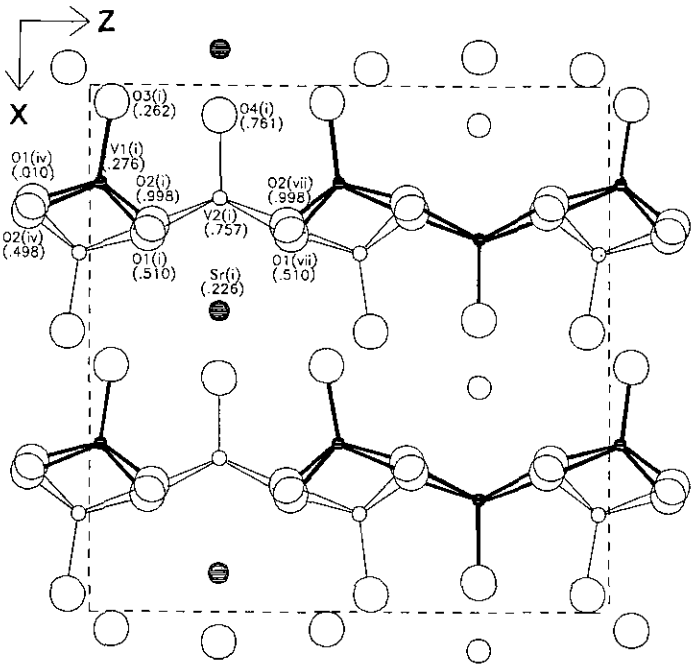

FIG. 4. Projection of the crystal structure of SrV_3O_7 down the *b*-axis. Large circles represent the O atoms, the small circles V atoms, and medium-sized circles Sr atoms. Numbers beneath atom labels are *y*-coordinates.

the susceptibility data can not be fitted to a 2-D Heisenberg model satisfactorily. Among the three simple models tested, a dimer, 1-D and 2-D Heisenberg, only the $S = \frac{1}{2}$ 1-D (infinite linear chain) model gives a relatively good fit to the observed data. The equation we used for the 1-D fit can be written as

$$\chi_m = \frac{N\bar{g}^2\mu_B^2}{kT} \cdot \frac{A + BX^{-1} + CX^{-2}}{1 + DX^{-1} + EX^{-2} + FX^{-3}} + \chi_{TIP} + \frac{C}{T - \theta},$$

where $X = kT/|J|$, $\bar{g}$ is the powder-averaged *g*-factor, and *J* the exchange constant. The first term is from Hatfield (*16*) and it evaluates the susceptibility for a 1-D $S = \frac{1}{2}$ Heisenberg system. The last two terms correct for temperature independent contributions and those from paramagnetic impurities when necessary. The following coefficients which were obtained from a fit of the 1-D equation to a theoretical calculation for the $S = \frac{1}{2}$ Heisenberg system (*16*) were used in our calculation: $A = 0.25$, $B = 0.14995$, $C = 0.30094$, $D = 1.9862$, $E = 0.68854$, $F = 6.0626$. The high-temperature paramagnetic range was fitted to the Curie–Weiss law. Relevant parameters are listed in Table V except for SrV_3O_7 where insufficient high-temperature data were available. The θ_c values are all large and negative while the Curie constants are slightly larger than the theoretically upper limit for a d^1 ion, 0.37 K · cm^3 · $mole^{-1}$. Again, this may be due to the use of a truncated data set or might reflect a small contamination by V^{3+} which appears to be possible from the TGA data. The observed and calculated susceptibility values in the low temperature range for CdV_3O_7,

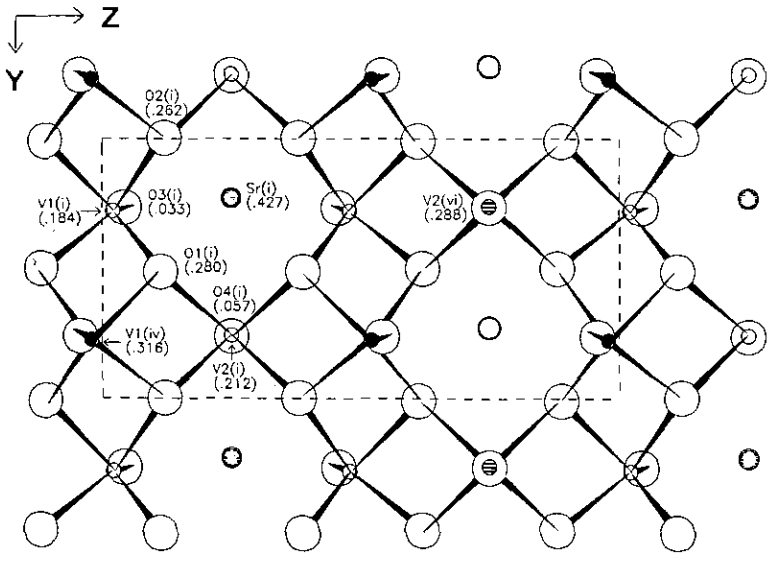

FIG. 5. Projection of the crystal structure of SrV_3O_7 down the a-axis. Atom projection conventions are the same as those in Fig. 4. Numbers beneath atom labels are x-coordinates.

CaV_3O_7 and SrV_3O_7 are plotted in Figs. 6, 7, and 8, respectively. In all cases the fitting failed to reproduce the position of the magnetic susceptibility maximum and always gave higher values, but the basic shape of the susceptibility curve seems correct. This indicates that the real magnetic behavior is probably more complicated than that which a simple 1-D Heisenberg model can describe as is not surprising given the quasi-two-dimensional structure and perhaps the possibility that the g-factors may be somewhat anisotropic.

Several other features are worth noting in the susceptibility vs temperature plots. Details of the low temperature range can be seen in Fig. 8 and the inserts in Figs. 6 and 7. Note the sharp maximum at 22 K for

TABLE V

MAGNETIC DATA FOR MV_3O_7 (M = Cd, Ca, Sr)

Parameter \ MV_3O_7		CdV_3O_7	CaV_3O_7	SrV_3O_7
$r(M^{2+})$(CN = 7, Å) (19)		1.17	1.20	1.35
$T(\chi_{MAX})$ (K)		35	80	110
1-D fit	g	1.43	1.82	1.80
	J/k (K)	−37.0	−76.6	−95.5
	χ_{TIP}(cm^3 · mole^{-1})	3.6×10^{-4}	—	—
Curie–Weiss law fit	Temp. range (K)	100–290	120–300	—
	C (K · cm^3 · mole^{-1})	0.408	0.444	—
	θ_c (K)	−154	−253	—

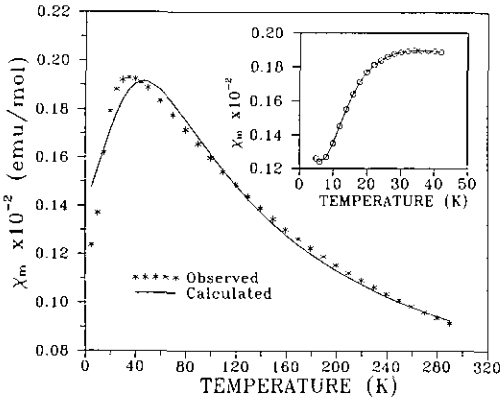

FIG. 6. Magnetic susceptibility per mole V as a function of temperature for CdV_3O_7. The calculated curve is based on a fit to an $S = \frac{1}{2}$ Heisenberg infinite chain model. The insert in the upper right displays the observed curve only.

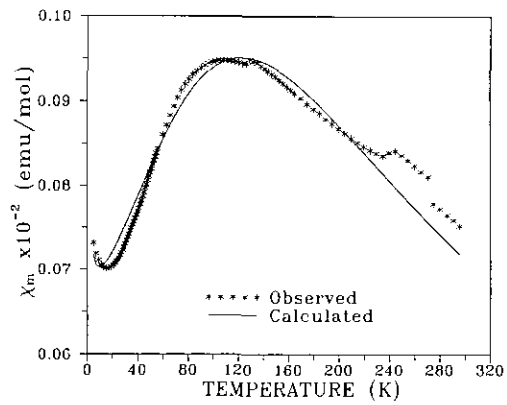

FIG. 8. Magnetic susceptibility per mole V as a function of temperature for SrV_3O_7. The calculated curve is based on a fit to an $S = \frac{1}{2}$ Heisenberg infinite chain model.

CaV_3O_7 which likely indicates the onset of *three-dimensional long-range order, while* no such feature is seen for CdV_3O_7 and SrV_3O_7. Thus it is difficult to conclude if there is any long-range magnetic order for these two compounds from the susceptibility data. The magnetic behavior of SrV_3O_7 is complex. Besides the most prominent broad maximum at ~110 K, two more smaller maxima near 130 and 240 K were observed. The features below 270 K are reproducible. The sudden drop near 280 K is a random instrumental error typical of the SQUID magnetometer we used because three independent measurements in that temperature range gave three different results. A similar problem had been observed occasionally for other compounds, too. The solid curve in Fig. 8 was calculated based on parameters fitted only in the temperature range 5–240 K and then extrapolated to 300 K. Although the possibility of contributions from other impurities can not be ruled out, it is likely that the magnetic behavior of SrV_3O_7 is more complex than that of CdV_3O_7 and CaV_3O_7 since the V–O square pyramids of SrV_3O_7 are more highly distorted as discussed above. Single crystals would probably help to determine its magnetic behavior definitively.

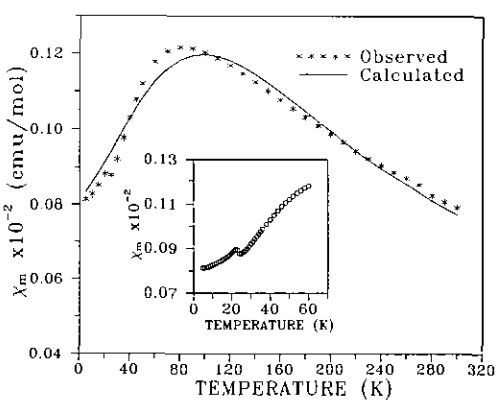

FIG. 7. Magnetic susceptibility per mole V as a function of temperature for CaV_3O_7. The calculated curve is based on a fit to an $S = \frac{1}{2}$ Heisenberg infinite chain model. The insert in the lower part displays the observed curve only.

Since these materials are insulators, the appearance of antiferromagnetism must involve V–O–V superexchange interactions. Superexchange interactions are known to be dependent on both the distance between magnetic ions and the angles involved in

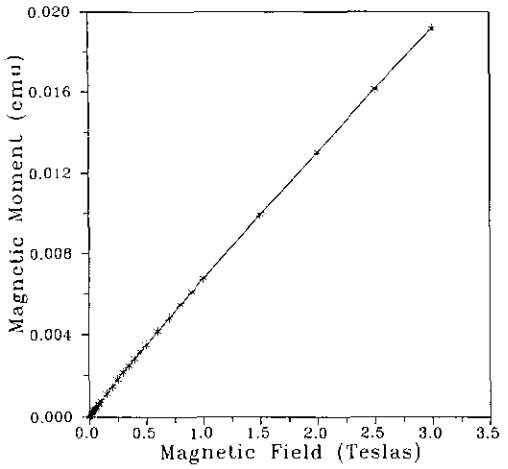

FIG. 9. Change in magnetic moment of CdV_3O_7 as a function of applied magnetic field at 7 K. Sample mass = 0.0819 g.

the paths. Even though the magnetic data suggest a one-dimensional character, it is not clear which path is responsible for the observed magnetic behavior. As discussed above, there are two possible ways of viewing the chains. Both involve V–O–V bonds, and the V–V distances in both directions ($V(1)^{i}$–$V(1)^{iv}$ and $V(1)^{i}$–$V(2)^{vi}$) are nearly equal, as can be seen from Table IV. Besides, there is no regular change in either the V–V distances or V–O–V angles from CdV_3O_7 to SrV_3O_7. The systematic increase in coupling constant $|J|$ with increasing size and thus increasing basicity of M^{2+} in MV_3O_7 are likely traceable to an inductive mechanism. That is, there exists a competition between the M^{2+} ion and the V(IV) for the oxygen electron density associated with the O(1) and O(2) atoms in the basal plane of the VO_5^{6-} pyramids which are involved in the superexchange pathway. Thus the strength of the M^{2+}–O(1), O(2) interaction will have an inverse effect on the strength of the V–O–V superexchange interaction. The importance of the M^{2+}–O(1), O(2) interaction should decrease with increasing basicity of M^{2+}, which is the observed trend.

In addition to short-range magnetic correlations as discussed above, there is clear evidence for long-range magnetic order in at least two of these compounds, CaV_3O_7 and SrV_3O_7. For CaV_3O_7, the susceptibility cusp at 22 K is indicative as are the data of Fig. 10, which show clear evidence of a spin flop transition in the 5-K data. A similar curve is seen in Fig. 11 for SrV_3O_7 at 15 K, but no firm evidence exists for CdV_3O_7.

Both V(IV) and Cu(II) oxides with square pyramidal metal–oxygen polyhedra and layered crystal structures show evidence for low-dimensional magnetic correlations. For example in $YBa_2Cu_3O_{6+x}$ with x near zero, evidence for short-range order is found up to quite high temperatures (*17*). The intra planar exchange constant is estimated to be of the order $|J_{intra}|/k \approx 10^3$ K. In the V(IV) oxides studied here the short-range exchange is an order of magnitude weaker with the largest value for SrV_3O_7 of $|J|/k \approx 100$ K.

There exist of course significant differences in molecular and electronic structure of MO_5 square pyramids for M = V(IV) and Cu(II). In the copper oxides the metal atom

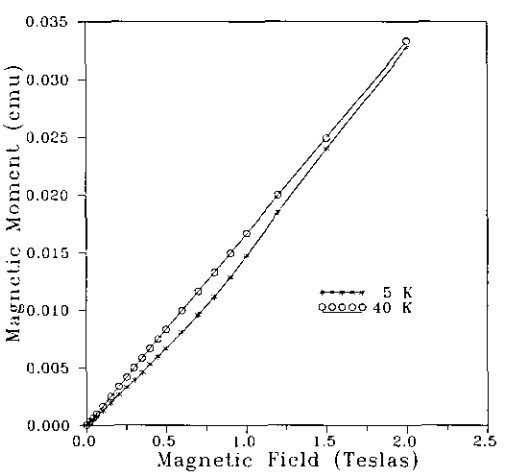

FIG. 10. Change in magnetic moment of CaV_3O_7 as a function of applied magnetic field at 5 and 40 K. Sample mass = 0.1704 g.

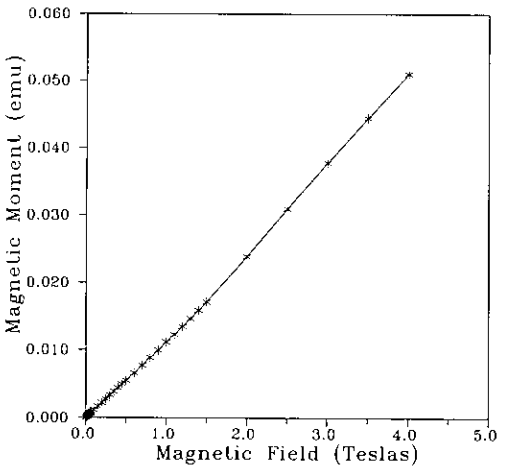

FIG. 11. Change in magnetic moment of SrV_3O_7 as a function of applied magnetic field at 15 K. Sample mass = 0.1980 g.

is nearly coplanar with the four basal oxygens, and the fifth Cu–O bond is significantly longer. In $YBa_2Cu_3O_{6.2}$, for example, the Cu-atom is only 0.23 Å above the oxygen plane with four Cu–O distances of 1.945 Å and the axial Cu–O at 2.437(5) Å (*18*). By contrast, in SrV_3O_7 the axial V–O distance, 1.616(9) Å, is shorter than the mean V–O distances to the pyramid base, 1.97(2) Å. This of course reflects the V=O or vanadyl character of the axial bond.

As a result the V–O–V angles which are crucial to superexchange range between 125° and 138° for V(1)–O(1, 2)–V(2) links along the *c*-axis direction and 98°–102° for V(1)–O(1)–V(1) and V(1)–O(2)–V(2) links along the *b*-direction. In $YBa_2Cu_3O_{6.2}$ the Cu–O–Cu angles within the planes are all around 166° (*18*). In the copper oxides the single hole occupies an orbital of $d_{x^2-y^2}$ symmetry, while in the vanadium oxides the single electron resides in a d_{xy} orbital. The former situation represents σ-symmetry while the latter, π-symmetry with respect to the metal–ligand interaction. Both the bond angle and orbital symmetry situations favor a considerably stronger short-range exchange interaction in the copper oxides, although it is difficult to quantify the difference.

Acknowledgments

We gratefully acknowledge the financial support of the Natural Science and Engineering Research Council of Canada and the Ontario Centre for Materials Research. We thank Professor C. V. Stager for use of the magnetometer and Mr. F. Gibbs for obtaining the TGA data.

References

1. J. B. GOODENOUGH, A. MANTHIRAM, AND G. DUTTA, *Eur. J. Solid State Inorg. Chem.* **28,** 1125 (1991).
2. M. J. REY, PH. DEHAUDT, J. C. JOUBERT, B. LAMBERT-ANDRON, M. CYROT, AND CYROT-LACKMANN, *J. Solid State Chem.* **86,** 101 (1990).
3. A. NOZAKI, H. YOSHIKAWA, T. WADA, H. YAMAUCHI, AND S. TANAKA, *Phys. Rev. B* **43,** 181 (1991).
4. M. CYROT, B. LAMBERT-ANDRON, J. L. SOUBEYROUX, M. J. REY, PH. DEHAUHT, F. CYROT-LACKMANN, G. FOURCAUDOT, J. BEILLE, AND J. L. THOLENCE, *J. Solid State Chem.* **85,** 321 (1990).
5. M. ITOH, M. SHIKANO, R. LIANG, H. KAWAJI, AND T. NAKAMURA, *J. Solid State Chem.* **88,** 597 (1990).
6. W. GONG, J. S. XUE, AND J. E. GREEDAN, *J. Solid State Chem.* **91,** 180 (1991).
7. W. GONG, J. E. GREEDAN, G. LIU, AND M. BJORGVINSSON, *J. Solid State Chem.* **95,** 213 (1991).
8. GUO LIU, AND J. E. GREEDAN, submitted for publication.
9. J.-C. BOULOUX, AND J. GALY, *Acta Crystallogr. Sect. B* **29,** 269 (1973).
10. J.-C. BOULOUX, AND J. GALY, *Acta Crystallogr. Sect. B* **29,** 1335 (1973).
11. J.-C. BOULOUX, AND J. GALY, *J. Solid State Chem.* **16,** 385 (1976).
12. See, for example, J. F. BRINGLEY, S. S. TRAIL, AND B. A. SCOTT, *J. Solid State Chem.* **86,** 310 (1990).
13. R. J. HILL, AND C. J. HOWARD, Australian Atomic Energy Commission Report No. M112, Lucos Heights Research Laboratories, New South Wales, Australia (1986).
14. D. B. WILES, AND R. A. YOUNG, *J. Appl. Crystallogr.* **14,** 149 (1981).

15. J. N. Reimers, J. E. Greedan, and M. Sato, *J. Solid State Chem.* **72,** 390 (1988).
16. W. E. Hatfield, *J. Appl. Phys.* **52,** 1985 (1981).
17. D. C. Johnston, S. K. Sinha, A. J. Jacobson, and J. M. Newsam, *Physica C* **153–155,** Pt. 1, 572 (1988).
18. K. Kamarás, C. D. Porter, M. G. Doss, S. L. Herr, D. B. Tanner, D. A. Bonn, J. E. Greedan, A. H. O'Reilly, C. V. Stager, and T. Timusk, *Phys. Rev. Lett.* **59,** 919 (1987).
19. R. D. Shannon, *Acta Crystallogr. Sect. A* **32,** 751 (1976).